THE ROYAL SOCIETY

New direct observations of crack closure processes in Al–Li 2090 T8E41

By A. Guvenilir[1]†, T. M. Breunig[1]‡, J. H. Kinney[2] and S. R. Stock[1]

[1]*School of Materials Science and Engineering and Mechanical Properties Research Laboratory, 778 Atlantic Avenue, Georgia Institute of Technology, Atlanta, GA 30332-0245, USA* (stuart.stock@mse.gatech.edu)

[2]*Chemistry and Materials Science Department, Lawrence Livermore National Laboratory, Livermore, CA 94550, USA*

Earlier, crack opening as a function of position within an optically opaque notched tensile sample (NT-3) of Al–Li 2090 was reported for four loads by Guvenilir and co-workers; these measurements were made with high-resolution X-ray computed tomography. This paper reports the same type of results for a second notched tensile sample (NT-4): the authors believe this to be the second sample whose crack closure was quantified as a function of position. The crack within NT-4 was found to be more planar than, and to close differently to, that in NT-3. In NT-4, the crack 'zipped' shut from the tip; this is in contrast to the earlier results on the asperity-dominated crack in NT-3, where contact occurred primarily behind the open crack tip. During unloading of NT-4, the crack faces came into contact above the closure load defined by the intersection of tangent lines to the upper and lower portions of the load–deflection curve; this is similar to previous observations in sample NT-3. Estimates of $\mathrm{d}a/\mathrm{d}N$ as a function of ΔK for samples NT-3 and NT-4 agree with others' measurements, which suggests that the closure observations of this paper also apply to compact tension samples of Al–Li 2090.

Keywords: aluminium; crack closure; fatigue; X-ray computed tomography; crackface geometry

1. Impact of Professor Lang

One of the authors (S.R.S.) owes his interest in X-radiation for volumetric materials studies to Professor Lang's work on section topography of perfect crystals, which clearly demonstrated how X-rays could be used to measure three-dimensional properties. This author's first personal encounter with Professor Lang (Durham NATO ASI) emphasized how much important information could be obtained through detailed analysis of the spatial distribution of diffracted intensity recorded on topographs; a subsequent visit to Professor Lang's laboratory confirmed the strong impression.

† Present address: Motorola, Yield Enhancement Technology Transfer, 3501 Ed Bluestein Boulevard, Austin, TX 78721, USA.

‡ Present address: Department of Restorative Dentistry, University of California, San Francisco, CA 94143-0758, USA.

This type of analysis kindled the aforementioned author's interest in X-ray diffraction imaging and in absorption imaging (X-radiography), which later extended to high-resolution X-ray computed tomography. Thus, even though the present work does not concern diffraction imaging or crystal characterization, it is, in a very real sense, an outgrowth of Professor Lang's work. Professor Lang's X-ray transmission topographs and their interpretation have been (and will continue to be) a severe standard against which other X-ray imaging work is measured.

2. Introduction

Different Al alloys show substantial variation in fatigue crack propagation rates, and sometimes these differences are due to one of several fatigue crack closure processes (Christensen 1963; Elber 1971; Suresh & Ritchie 1982). Considerable variability in macroscopic closure measurements has been reported, and these results appear to depend on factors such as where the displacements are measured (Macha *et al*. 1979; Fine *et al*. 1984; Tokaji *et al*. 1984). The questions of how closure should be measured and how the resulting measurements should be interpreted remain open.

One alloy showing large crack closure effects is Al–Li 2090 T8E41, and the extremely low crack propagation rates measured for certain orientations have been linked to the texture-induced crack roughness (Yoder *et al*. 1988). Recently, very-high-resolution X-ray computed tomography (i.e. X-ray tomographic microscopy or XTM) has been used to image a fatigue crack within the interior of a notched tensile sample from the centre of a plate of Al–Li 2090 T8E41 (Breunig *et al*. 1992; Stock *et al*. 1995*a*), and crack opening as a function of position across the crack face was measured for four different loads and related to the three-dimensional crack-face geometry and to the closure stress intensity (Guvenilir *et al*. 1997). Similar high-resolution X-ray computed tomography work on damage quantification in monofilament SiC/Al (Breunig 1992), and on porosity distribution in chemical vapour infiltrated SiC/SiC composites (Kinney *et al*. 1993; Lee *et al*. 1998), reinforces confidence in the crack closure results obtained with high-resolution X-ray computed tomography.

This paper describes detailed results of very-high-resolution X-ray computed tomography on a second notched tensile sample (NT-4) of Al–Li 2090 T8E41. Like the first sample studied (NT-3), the specimen discussed here is reconstructed with 6 μm voxels (volume elements), and crack opening is quantified as a function of position with sensitivity to changes in crack opening approaching 0.6 μm. As in the first report, the spatial distribution of crack opening is related to the three-dimensional crack-face geometry and the load–displacement curve for the cracked sample, and these results are then related to what was reported earlier. Estimates of the stress intensity range and of fatigue crack propagation rates for the two notched tensile samples studied with X-ray tomography are also compared with what has been reported by others in compact tension samples of this alloy (Pao *et al*. 1989; Venkateswara Rao *et al*. 1988*a*). In the interest of brevity, many of the data collection and analysis methods reported earlier are abbreviated here, but they can be found elsewhere (Breunig *et al*. 1992, 1993; Guvenilir *et al*. 1994, 1997; Guvenilir 1995; Stock *et al*. 1995*a*).

3. Experimental procedures

The notched tensile sample was machined from the centre of the highly textured 12.5 mm thick plate of Al–Li 2090 (Breunig *et al*. 1992); the diameter (D) of the

sample was 2.9 mm, and the notch had a diameter (d) of 1.9 mm. The gauge section and the total length of the sample were 15.9 mm and 30.6 mm, respectively, and the sample was loaded in the rolling direction (L) of the plate. The scaling and tolerances for the samples were according to ASTM standard E-602-81, and this scaled version allows reasonable X-ray transmissivity and tomographic sensitivity for X-ray photons with energies between 20 and 25 keV (i.e. $\mu T \leqslant 2$, where μ is the linear attenuation coefficient, and T is the maximum X-ray path length through the sample). Mechanical testing was done in load control in a standard servohydraulic fatigue machine at 22 °C with $R = \sigma_{\min}/\sigma_{\max} = 0.1$ and a 5 Hz haversine waveform. The maximum load was 54.5 kg during the initial 18 000 cycles, was decreased to 50 kg through 30 500 cycles, and lowered to 45 kg until crack growth ended after 34 760 cycles. The change in displacement as a function of load was monitored with a clip gauge at the mouth of the notch, and the change in compliance was used to follow crack extension.

The Lawrence Livermore XTM apparatus (Kinney & Nichols 1992) and a portable load frame (Breunig *et al*. 1993) were used for *in situ* imaging of the crack as a function of applied load. The sample was positioned approximately 23 m from the X-ray source at beamline A-2 of the Cornell High Energy Synchrotron Source and as close as possible to the two-dimensional X-ray detector (i.e. within several mm). The resulting sample–detector separation was about 5.0 cm. Monochromatic 22 keV X-rays from an Si(111) monochromator system were used to image the sample. Approximately 3500–4000 photons per pixel were collected in the most heavily exposed pixels, and this required between 2 and 5 s.

Two sets of data, each simulating the unloading portion of a fatigue cycle, were collected from the volume surrounding the notch. Ordinarily, a sample would be imaged in a single sequence of loads (i.e. from highest to lowest load), but here the measurements were split into two parts to ensure that the entire load–displacement curve would be spanned if, midway through the experiment, there was catastrophic synchrotron storage ring or imaging apparatus failure. The first dataset was acquired between the maximum load used during crack growth and 20% of the maximum load (i.e. five loads from 45 kg to 9 kg at intervals of 9 kg). The second dataset started at 90% of, and finished at 10% of, the maximum load used during the mechanical testing (i.e. 40.5 kg to 4.5 kg, at intervals of 9 kg). Only the first dataset will be discussed here since the second set revealed little that was not seen in the first set. The filtered back-projection algorithm (Herman 1980; Kak & Slaney 1988) was used to reconstruct the slices making up the volume of the sample containing the crack; each voxel was $(6.4\,\mu\mathrm{m})^3$.

The opening of the three-dimensional crack was analysed using cuts perpendicular to the reconstructed slices, i.e. along the loading direction; this has been found to be a more robust procedure than measuring opening within slices. First, the average linear attenuation coefficient for the matrix μ_{avg} was measured for each load in a volume away from both the crack and the edge of the sample. Second, a threshold value $\mu_{\mathrm{th}} = 0.9\mu_{\mathrm{avg}}$ was calculated for each load. Next, the approximate position of the crack was marked at several positions in each cut, and, with this guidance, a computer routine for quantifying crack opening located the crack and then searched from the centre of the crack along the loading axis until a voxel on both sides was encountered with $\mu > \mu_{\mathrm{th}}$, i.e. the limits of the crack. Neglecting the attenuation of air, the measured fraction of crack opening in a given voxel $\Delta V/V$ was the average

value of the attenuation coefficient in the specimen minus the value where the crack was open, divided by the average value of the attenuation coefficient:

$$\frac{\Delta V}{V} = -\frac{\mu_{\text{avg}} - \mu_{\text{obs}}}{\mu_{\text{avg}}}. \tag{3.1}$$

In the final step of the measurement process, the partial voxels comprising the crack (between the crack limits) were summed to give the total opening for that specific position within the sample.

One way of easily following the variation of crack opening within the sample is to project the amount of opening onto a plane perpendicular to the load axis, i.e. a plane parallel to the slice or reconstruction plane. This representation ignores the non-planarity of the crack, and, by making a separate measurement and projection for each load, it allows one to avoid three-dimensional registration (at different load levels) of the crack within a volume under different amounts of elastic distortion.

Once 'areas' of importance in the closure process were identified (i.e. positions where no changes in the opening are observed or where the greatest changes are seen), the full three-dimensional dataset was examined quantitatively. Three-dimensional renderings of the crack faces were combined with the measured openings and viewed from a number of different perspectives. This second step focused on geometrical effects, i.e. the crack closing first at certain microstructural features such as the sides of ridges, etc.

4. Results and discussion

Reconstructed slices from the same location in the specimen are shown in figure 1 for 45, 36, 27, 18 and 9 kg loads.† Darker pixels represent higher attenuation (i.e. a smaller fraction of the voxel occupied by crack), and the linear grey scale shows the percentage of the voxel occupied by the crack. The concentric rings seen in these slices are a reconstruction artefact resulting from uncorrected detector nonlinearities. Since these artefacts did not interfere with crack-opening measurements, these rings were not eliminated by image processing. The jagged crack intersects each slice at an irregular set of positions, and the crack becomes less clearly defined as the load decreases. A significant amount of physical crack closure, therefore, occurs before the minimum load has been reached.

In cuts parallel to the load axis, the non-planar behaviour of the crack becomes more distinct. Figure 2 shows a single 6.4 μm thick cut at the same five loads and with the same scale seen in figure 1. These cuts also reveal significant physical closure above the minimum load used during crack propagation. Well-defined asperities similar to those observed before (Yoder *et al*. 1988; Breunig *et al*. 1992; Haase *et al*. 1998) are seen in the cuts, and their heights are about 40 voxels (0.26 mm) parallel to the load axis.

For the five loads, the sample's linear attenuation coefficient μ_{avg} averaged $5.75 \pm 0.16\ \text{cm}^{-1}$ ($\pm\Sigma$, i.e. mean values plus or minus Σ, one standard deviation). At 22 keV, the linear attenuation coefficient is expected to be between 7.50 and $7.82\ \text{cm}^{-1}$. This difference is much larger than expected and appears to be due to the smaller amount of polycarbonate intercepted by the X-ray beam when imaging the sample

† An estimate of stress intensity for each load follows discussion of the crack shape.

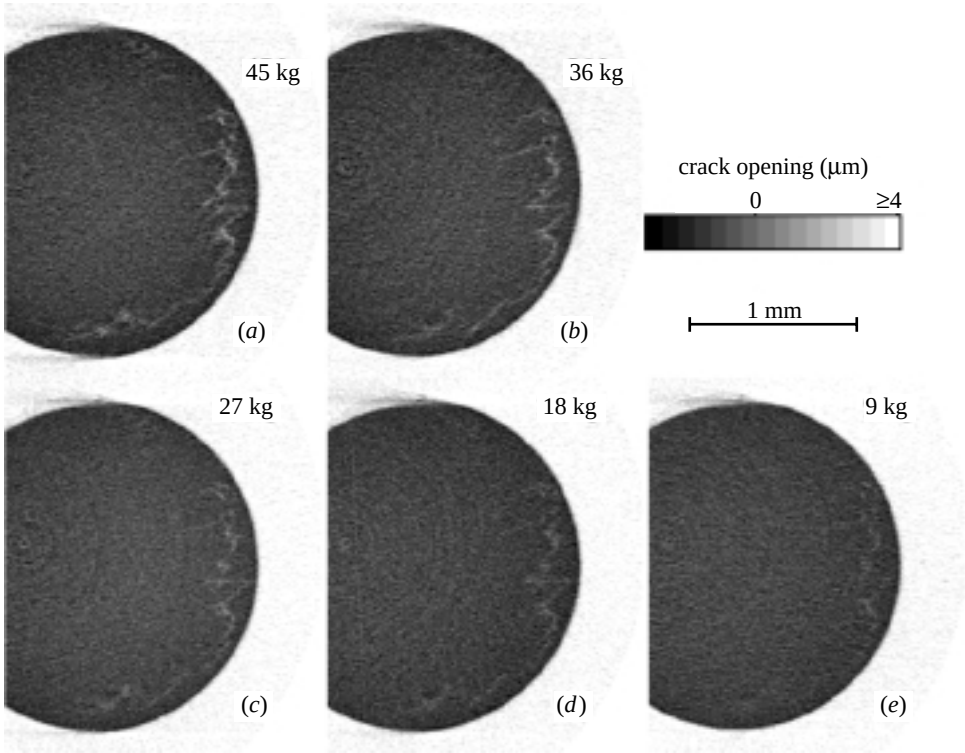

Figure 1. Slices from the same 6 μm thick section of the sample at 45, 36, 27, 18 and 9 kg loads ((*a*)–(*e*), respectively). The bar shows the crack opening associated with each grey level.

and the higher thickness where the reference data are obtained. This is a geometric consequence of using a somewhat, but not totally, X-ray transparent standoff to hold the grips of the load frame apart. Therefore, the sample appears to be less attenuating (relative to the 'incident' beam) than it actually is, and μ_{avg} is depressed for the reconstructed voxels. Another contribution to the difference could be the presence of higher-order harmonics in the beam. The difference between experimental and expected values does not, however, affect the crack-opening measurements, since the fraction of a voxel open is defined in terms of μ_{avg}.

At 45 kg, 26% of the approximately 69 000 voxels across the cross-section have $\mu < \mu_{\mathrm{th}}$ and are contiguous with the manually marked crack position. This fraction drops to 18% at 36 kg, decreases to 11% at 27 kg, remains nearly constant at 18 kg, and drops to 8% at 9 kg (figure 3). In addition to showing the fraction of voxels open as a function of applied load, figure 3 also shows $\langle O\rangle_{\mathrm{all}}$, the average opening for all voxels that were open at 45 kg, and $\langle O\rangle_{\mathrm{load}}$, the average opening of the subset of voxels that were open at a particular load. The third plot of figure 3 illustrates the decrease in O_{max}, the maximum opening of the crack. The lines in the plots are intended to help one follow the trends in the data and are not intended to suggest functional relationships.

At 45 kg, $\langle O\rangle_{\mathrm{all}} = \langle O\rangle_{\mathrm{load}} = 0.6$ voxel (4 μm) with a standard deviation of 0.2 voxel; $\langle O\rangle_{\mathrm{all}}$ decreases to 0.4, 0.2, 0.1 and 0.1 voxel for 36, 27, 18 and 9 kg loads,

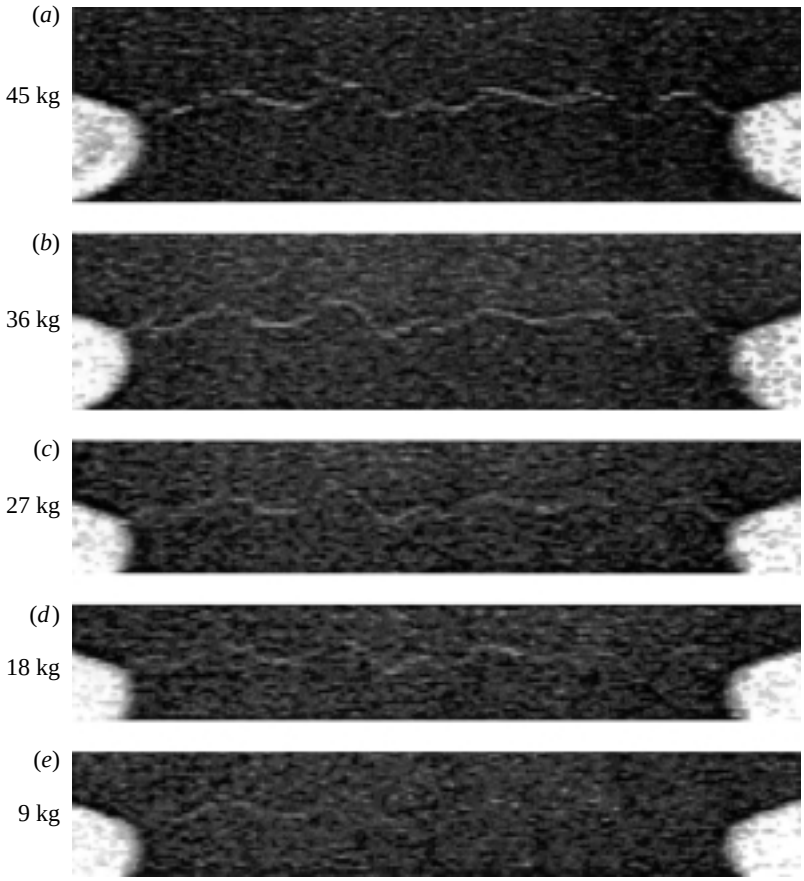

Figure 2. Cuts through the sample using the same grey scale as in figure 1 (from top to bottom 45, 36, 27, 18 and 9 kg loads). The notch is visible at the left and right of each image.

respectively. The standard deviation for each average opening was roughly constant and was 0.1 voxel. The mean crack opening of the voxels open at a particular load $\langle O \rangle_{\mathrm{load}}$ dropped from 0.6 voxel at 45 kg to 0.5, 0.5, 0.3 and 0.3 voxels for 36, 27, 18 and 9 kg loads, respectively; as one would expect, this is considerably less than that of $\langle O \rangle_{\mathrm{all}}$. Away from the edge of the sample, the maximum crack opening is 3.3 voxels at 45 kg and decreases to 2.4, 2.8, 1.5 and 1.7 voxels at 36, 27, 18 and 9 kg, respectively. Note that the maximum opening increases slightly at two points; these small changes are above the sensitivity limit of 0.1 voxel and could indicate lateral shifting of crack faces or could simply be incidental.

Histograms of the distribution of crack-opening values are shown in figure 4, and, as one would expect, the distribution of openings shifts to lower values with decreasing load. The magnitude of the shift is roughly constant from 45 to 36 kg and from 36 to 27 kg, but is much less for the loads below 27 kg. Note that the openings are shown only for those voxels open at 45 kg; by definition, there are no voxels with zero crack opening in the histogram at 45 kg.

In figure 5, the crack opening measured as a function of three-dimensional position

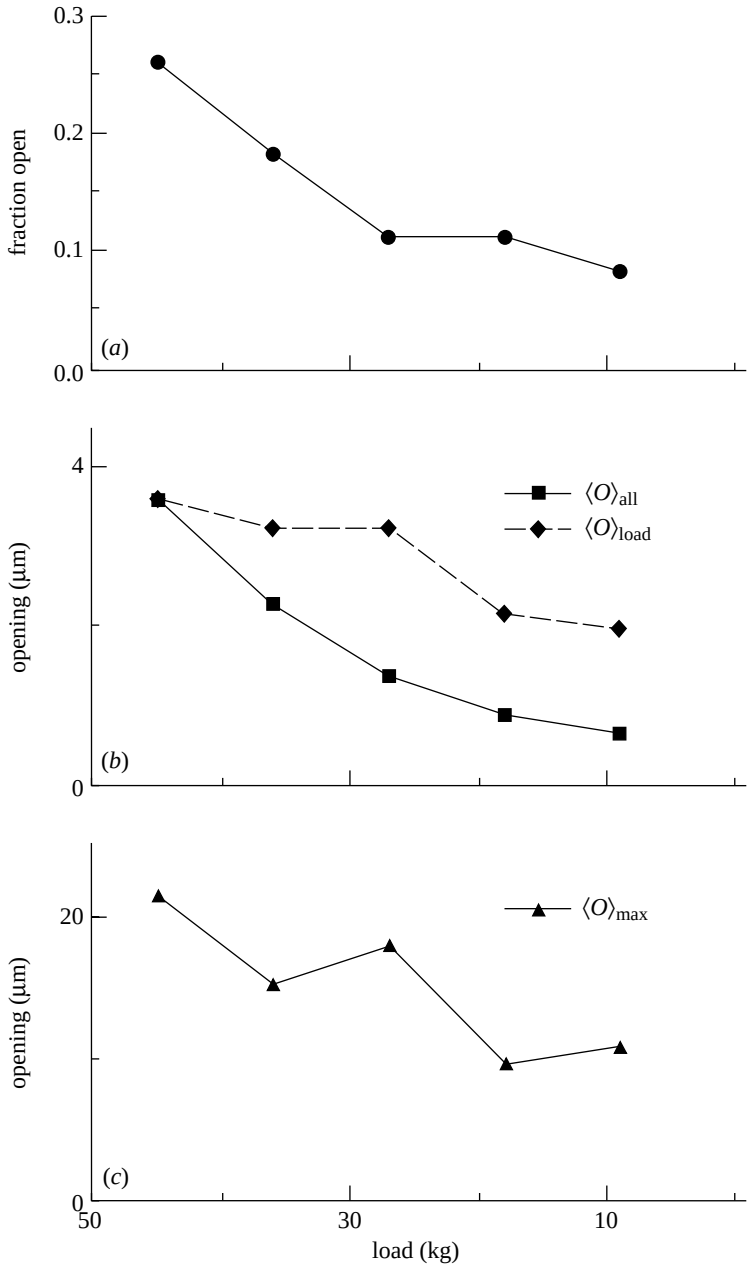

Figure 3. Fraction of the voxels in the sample's cross-section that are open (a); average opening for all voxels open at 45 kg $\langle O\rangle_{\mathrm{all}}$ and average opening for only those voxels open at each load $\langle O\rangle_{\mathrm{load}}$ (b); and maximum opening observed at each load O_{max} as a function of applied load.

is projected onto a plane perpendicular to the load axis; data for five loads are shown. The magnitude of opening is represented by colour: white pixels show the largest openings; red and magenta show the next largest openings; and blue, green

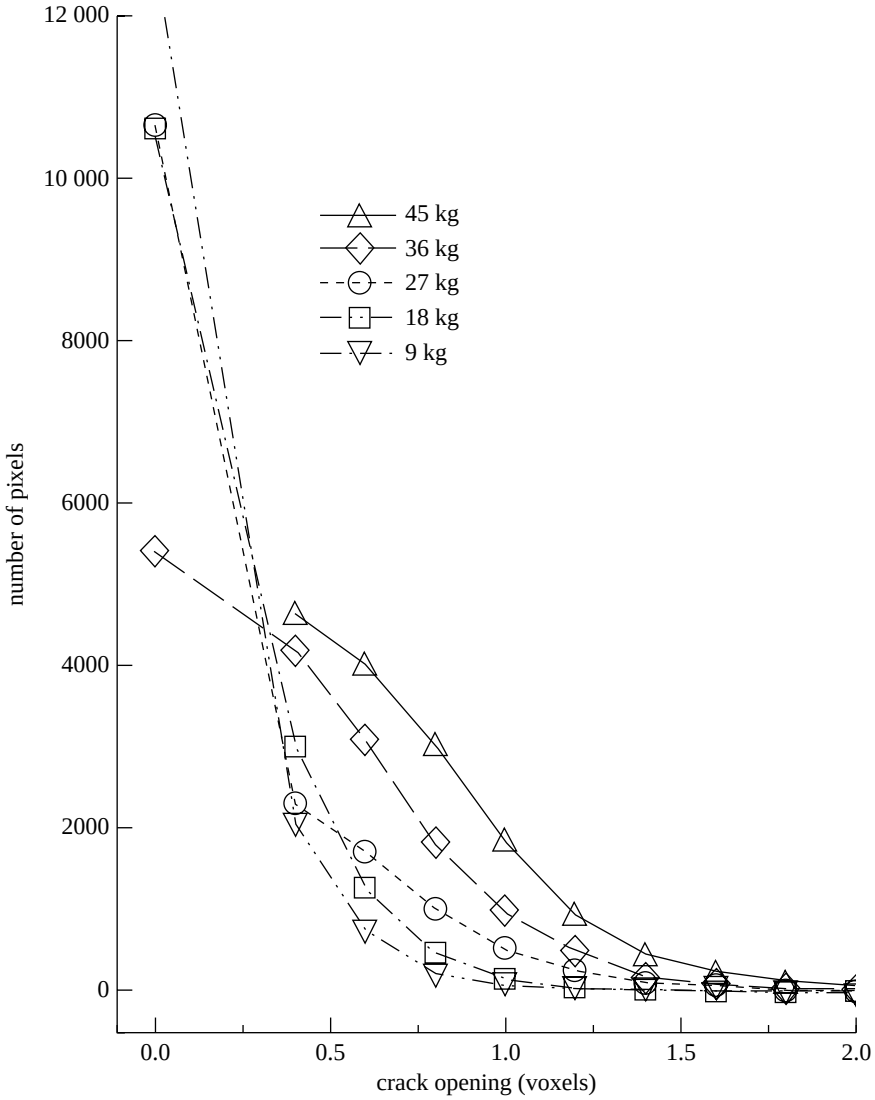

Figure 4. Histograms of crack openings for 45, 36, 27, 18 and 9 kg. Only those voxels that were open at 45 kg are included in this plot. In order to convert this plot to the total number of voxels with a given opening in the cross-section, 59 500 should be added to the number of voxels with zero opening.

and black pixels correspond to the smallest three increments of opening. The crack stretches almost half way around the sample, the crack's penetration into the sample is very irregular and the pattern of openings is quite complex.

The map of the projected openings can be divided into two parts: a thumbnail-shaped central region flanked by two 'tails' spreading part of the way around the sample's perimeter. The largest fraction of the crack's area is in the middle (thumbnail) portion of the crack. The two-dimensional projections of crack opening in figure 5 show that the crack stays open mostly in the middle region and that the apparent

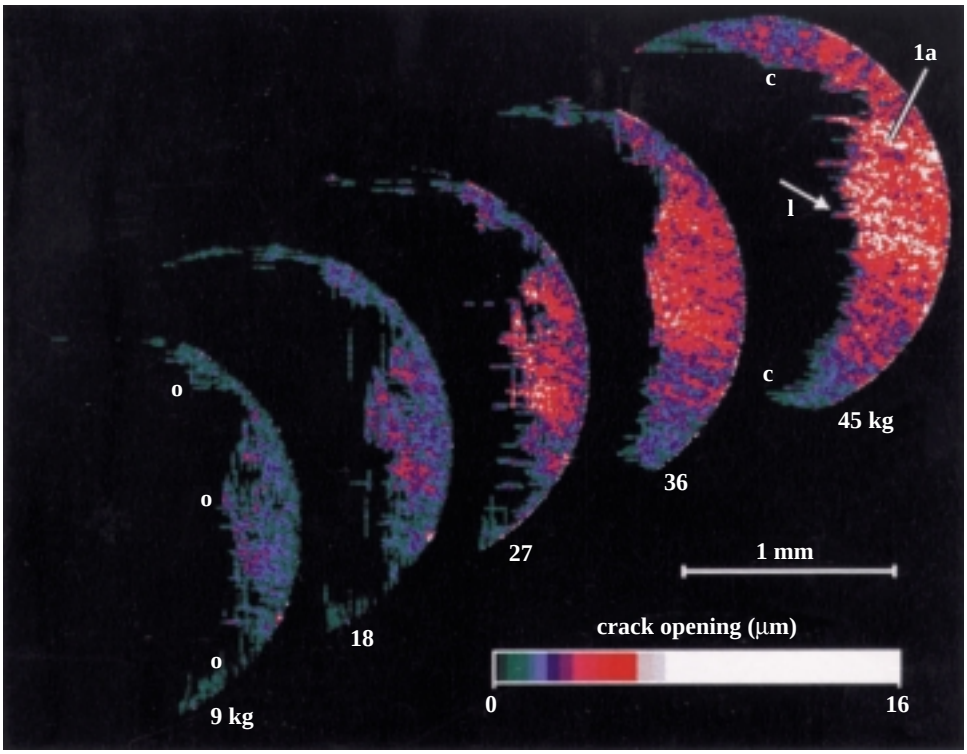

Figure 5. Crack opening as a function of position projected along the direction of the load axis onto a plane parallel to the slices. Each map of openings is labelled with the load at which it was obtained. The same colour table is used for all images: white for openings greater than 6.5 μm, intermediate openings (of the order of 5 μm) are shown as red, and decreasingly smaller openings are shown as blue, green or black, respectively. The features identified by letters are described in the text.

crack tip recedes most rapidly in the tails (especially the tail pictured uppermost in this figure). The region labelled 'c' in figure 5 closes most rapidly as the load is reduced, and the largest change in projected area between two loads occurs between 36 and 27 kg. Linear rows of voxels with large crack openings are observed at high loads (labelled 'l' in figure 5): as discussed below, this is an effect of crack surface geometry. As the load decreases, small pockets of open voxels remain even in the tails and near the crack tip; these pockets are indicated in the projected crack-opening image at 9 kg (labelled 'o' in figure 5). What makes these pockets stay open is not clear in these projections, but the three-dimensional images of the same data answer this question.

Figure 6 shows three views of the three-dimensional crack position within the sample; the horizontal planar mesh indicates uncracked material or the space outside the sample. The crack consists of three distinct regions, a relatively planar section in the middle, i.e. the thumbnail portion described in figure 5, and two jagged sections on either side, i.e. the tails identified in figure 5. The middle region of the crack is lower in physical height than the 'tail' regions in figure 6 and slopes gradually from the edge toward the centre of the sample (i.e. towards the crack tip). The middle

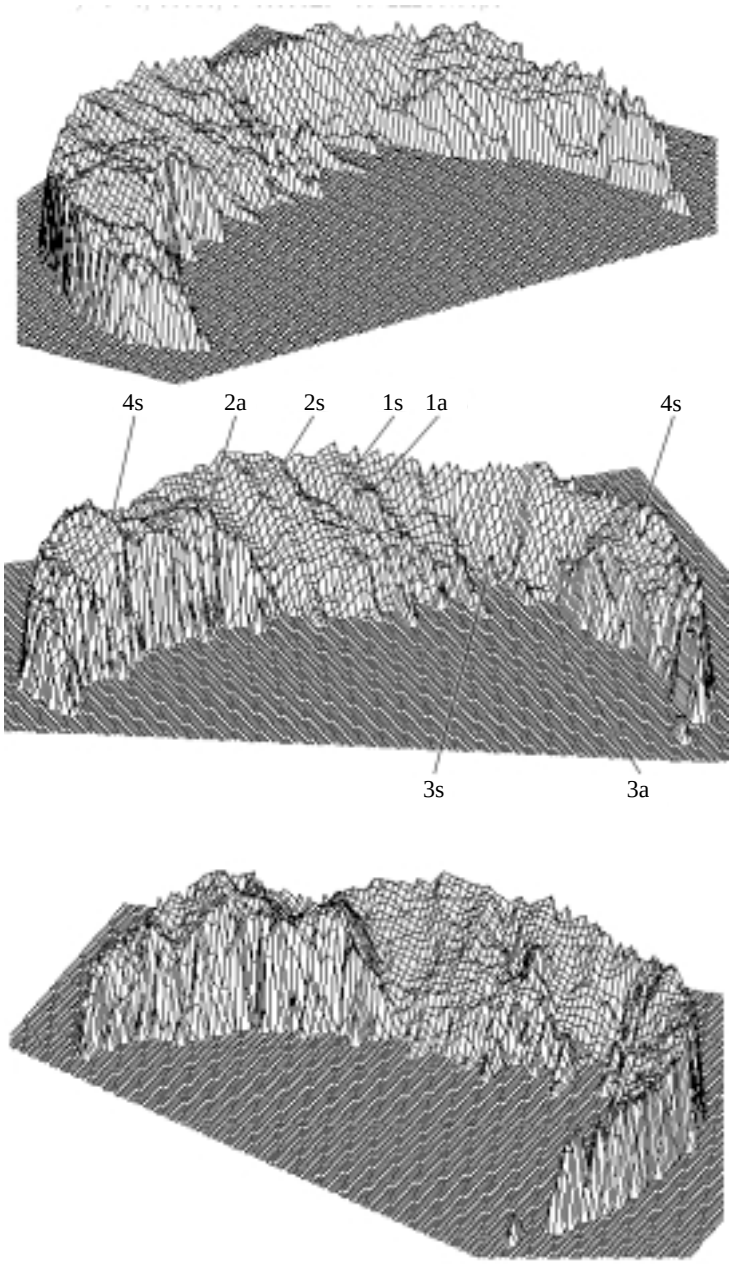

Figure 6. Three views of the crack from the centre of the sample. Three-dimensional mesh indicates the crack surface. The range of crack heights is 0.29 mm, and the diameter of the mesh is 1.9 mm.

region is relatively smooth with very few asperities projecting higher than 30 μm above their surroundings. In the two tails, however, the crack-face morphology is very different, consisting of sharp ridges running perpendicular to the crack front

(e.g. 4s in figure 6); these features are similar to delaminations. Unlike the middle region, the peaks of the ridges in the tails show a sharp downturn in the interior of the sample; these asperities are also much larger than those in the middle region, for example 4s in figure 6 compared with 1a in the middle region. In figure 6, the crack is viewed from the centre of the sample, and the left 'tail' corresponds to the lower portion of the two-dimensional projected crack-opening images in figure 5, and the right 'tail' represents the upper portion.

In figure 7, the measured crack opening (indicated by colour) for each x, y, z position is superimposed on a three-dimensional mesh plot of the crack face. The viewing perspective in figure 7 is the same as in the middle plot of figure 6. The greatest openings are shown in white or yellow, intermediate openings in orange and red, and the smallest openings in blue and black. The perspective is from the centre of the sample, and a separate plot is shown for each of the three highest loads.

As the load decreases from 45 kg, there are two types of contact in the middle region besides the retreat of the apparent crack tip. One type occurs at the asperities (i.e. at asperity peaks), which project upward from the fracture surface at least 5 pixels above their surroundings (i.e. '1a' in figures 6 and 7), and which are relatively far from the apparent crack tip. Asperity 1a resembles a spike protruding from the small ridge running from the edge of the sample to the crack tip. At 45 kg, the opening on the left flank of 1a was larger than that on the right flank. The opening on both sides is roughly equal at 36 kg, i.e. the left-hand side closed more rapidly than the right-hand side. Openings decreased by the same amount on both sides of 1a for loads below 36 kg. Near asperity 1a is a second smaller asperity labelled '1s'. The crack faces on either side of '1s' also close asymmetrically; the left-hand side closes before the right-hand side but the closure at 1s occurs at lower loads than does that at 1a. This suggests that the larger asperity shields the neighbouring smaller asperities, at least when the crack face is relatively smooth, and that some sliding must be occurring, perhaps due to a mismatch of fracture surfaces.

Figure 7 shows that the apparent crack tip in the tail regions recedes much more rapidly with applied load than it does in the less highly sloped middle region. In the middle region, the fracture surfaces contact at loads between 36 and 27 kg only on or around the larger asperities. Positions 2a and 2s, in the left tail region far from the crack tip, and 3a and 3s, at the border between the right tail and central regions near the crack tip, typify the asperity contacts in the tails, where the apparent crack tip recedes most rapidly along the large asperities.

In the neighbourhood of the larger asperities, small pockets of voxels remained open even at 9 kg. It also appears that contact on the large asperity ridges in the tails keeps the middle region of the crack more open than one would expect. At 9 kg, for example (figure 5), there are patches of open voxels in the thumbnail region near the crack tip (i.e. the original crack tip observed at maximum load) with openings as high as 0.5 voxel (3 μm), and there is very little change in the nominal position of the crack tip when the load is decreased from 18 to 9 kg. The pattern of openings and the pattern of contact are quite similar to those reported on the first notched tensile sample (Guvenilir *et al*. 1997).

The notch depth in sample NT-4 is 0.50 mm; and, from the computed tomography results, a_{m}, the maximum depth the crack penetrated into the sample, is an additional 75 voxels (0.48 mm). Thus, at 45 kg up to 26% of the sample diameter (at the tip of the notch) is occupied by the crack. At 36 kg the apparent crack tip has

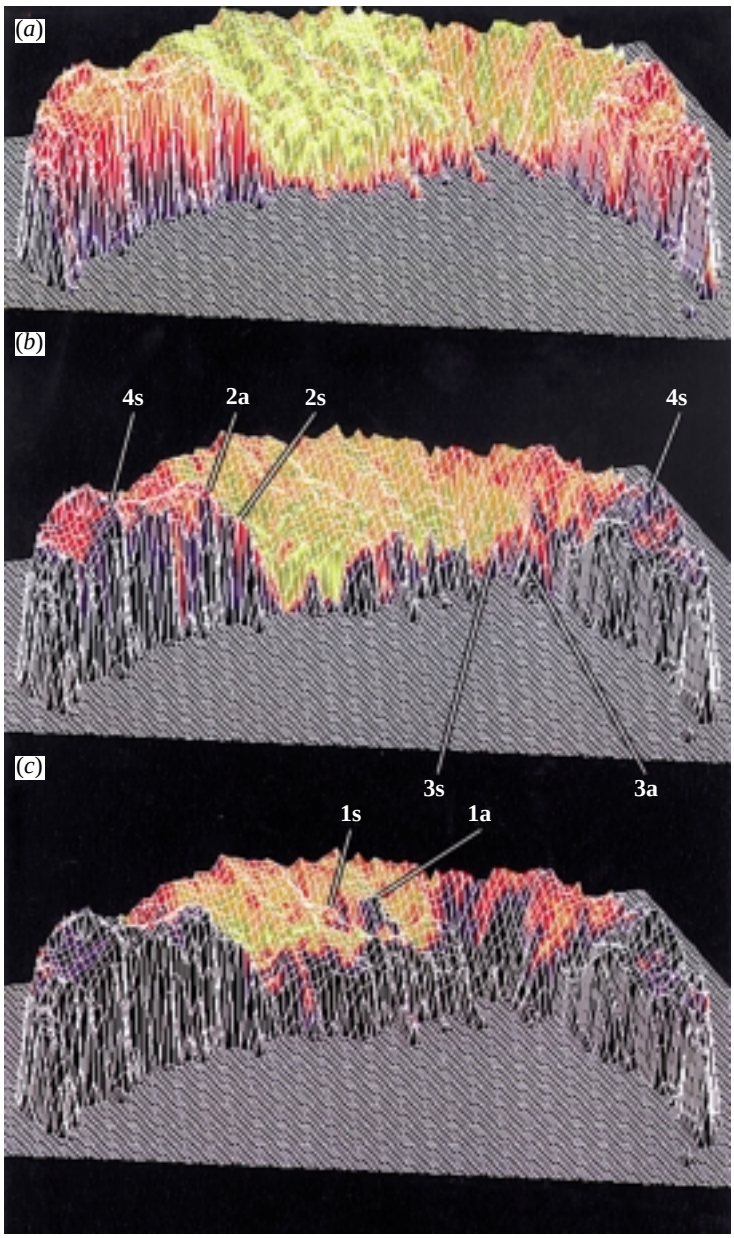

Figure 7. Crack opening related to the three-dimensional crack face. The top image shows crack opening at 45 kg superimposed on the mesh; the middle image shows opening at 36 kg superimposed on the mesh; and the bottom image shows opening at 27 kg superimposed on the mesh. The openings for all loads are shown on the same colour scale. Yellow represents openings of 13.5 μm or greater, and orange, red, purple, blue and black represent decreasing opening in this linear colour table. The horizontal and vertical size scales are identical. The features identified by letters are described in the text.

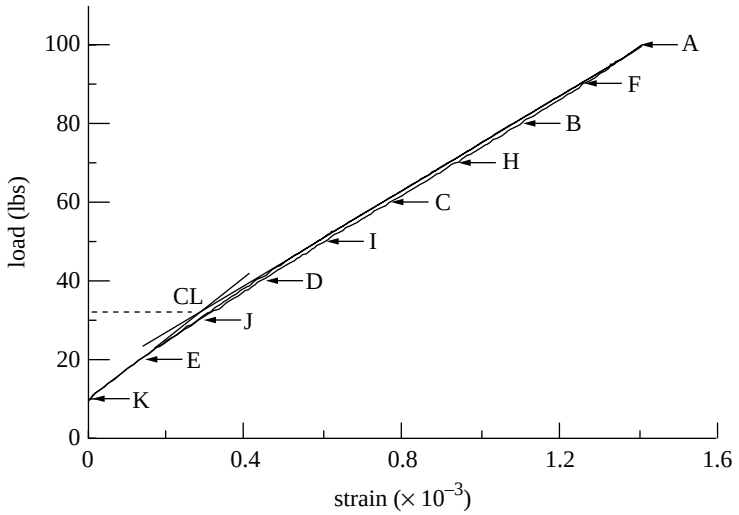

Figure 8. Load–displacement curve for sample NT-4, with the loads at which tomographic imaging was done indicated by letters A–E. The closure load, defined by tangents to the upper and lower portions of the curve, is about 15 kg.

retreated 5 voxels (i.e. to 0.45 mm from the notch tip), and at 27 kg, the additional retreat is 19 voxels (i.e. to 0.33 mm). At 18 kg the decrease is another 3 voxels, and at 9 kg the apparent crack tip is only 40 voxels from the notch tip.

The load–displacement curve for this sample (figure 8) was recorded after tomographic imaging was complete, and the five loads at which tomographic data were collected are indicated by the letters A–E. The intersection of tangents to the lower and upper portions of this load–displacement plot are taken to define the closure load; they cross at about 15 kg. The two- and three-dimensional crack-opening data (figures 5 and 7), as well as the fraction of crack opening, average crack-opening and histogram plots (figures 3 and 4), show, however, that the crack has closed significantly before the bend in the load–displacement curve.

While the average crack opening decreases fairly uniformly as a function of decreasing load, the fraction of open voxels decreases between all loads except 27 and 18 kg. This suggests that the change in slope of the load–displacement curve near 15 kg is not due to the change in average voxel opening or the change in fraction of voxels open. The correlation between *changing* slope (of the load–displacement curve) and relatively *unchanging* fraction of open voxels suggests that positions behind the crack tip where the crack was closed at 36 or 27 kg (i.e. before the bend in the load–deflection curve) begin to carry significant compressive load above 18 kg and are responsible for changing the sample's apparent stiffness. The two-dimensional projected crack-opening maps (figure 5), and crack opening as a function of three-dimensional crack position (figure 7), are also consistent with crack-face contact processes becoming increasingly important below 27 kg. It is expected, therefore, that the sample would appear to become stiffer during unloading from 27 to 9 kg, which would show up as a bend in the measured macroscopic load–displacement curve.

Comparing computed tomography results on notched tensile samples with the body of data in the literature requires estimation of crack growth rates and stress

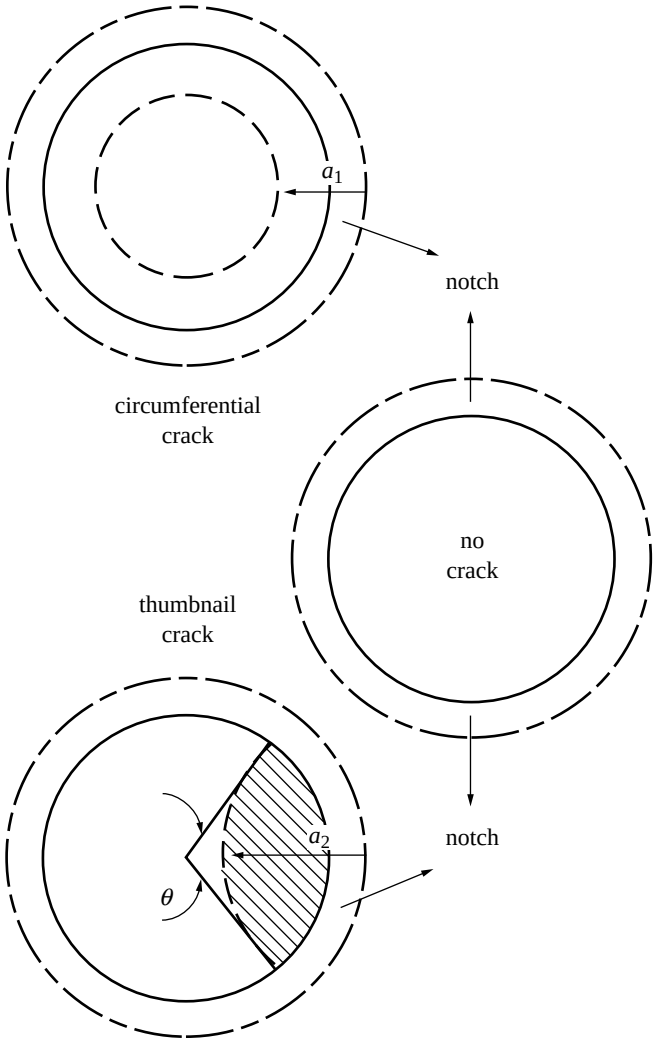

Figure 9. Schematic of geometries used for approximating the stress-intensity parameter for the crack in sample NT-4.

intensity parameters. A solution for the stress intensity factor for a thumbnail crack in a cylindrical notched sample is not available, to the best of the authors' knowledge, and obtaining such a solution for a non-planar thumbnail crack with tails extending along the outside of the sample is beyond the scope of the present study. Solutions exist for an external circumferential crack in a round bar (Tada *et al*. 1985; Erdogan 1982) and for a circular crack growing into a semi-infinite body (Tada *et al*. 1985; Newman & Raju 1981), and these can be used to approximate the stress intensity in notched tensile samples,

$$K = \sigma(\pi a)^{1/2} F, \tag{4.1}$$

where $\sigma = P/A_0$; P is the applied load, A_0 is the cross-sectional area, a is the crack

length, and

$$F = F\left(\frac{a}{r}\right) = \left[1 - \left(\frac{a}{r}\right)\right]^{-3/2}\left[1.122 - 1.302\left(\frac{a}{r}\right) + 0.988\left(\frac{a}{r}\right)^2 - 0.308\left(\frac{a}{r}\right)^3\right] \tag{4.2}$$

for a circumferential crack in a round bar of radius r, and

$$F = 2F_\theta = (2/\pi)(1.211 - 0.186\sin\theta) \tag{4.3}$$

for a position on a circular crack defined by the angle θ that the crack front makes relative to the sample surface. Note that the range of validity for F_θ is $10° < \theta < 170°$, and the maximum value of F_θ is 1.176. The corresponding stress intensity ranges ΔK are found by replacing σ with

$$\Delta\sigma = \frac{\Delta P}{A_0} = \frac{P_{\max} - P_{\min}}{A_0}. \tag{4.4}$$

Figure 9 illustrates each of these geometries: the dashed line indicates the unnotched diameter of the sample and the solid line the tip of the notch. Subscripts denote which crack length is being described: a_1 for the circumferential crack and a_2 for the thumbnail crack.

The geometry of sample NT-4, discussed above, is closest to the circumferential crack, and a rough estimate for the stress intensity can be obtained by approximating the crescent-shaped crack with depth a_{m} from the notch tip by a circumferential crack extending $a_{\mathrm{m}}/2$ from each point of the circumferential notch tip. In other words, the estimate is given by a circumferential crack of 0.74 mm depth in the 2.9 mm diameter sample. For 45, 36, 27, 18 and 9 kg loads, one estimates that $K = 6.4$, 5.1, 3.8, 2.5 and 1.3 MPa $\mathrm{m}^{-1/2}$, respectively, and the closure load of 15 kg corresponds to $K_{\mathrm{cl}} = 1.9$ MPa $\mathrm{m}^{-1/2}$.

A clip gauge was used to follow the change in compliance during fatigue crack growth of all of the notched tensile samples tested. What is measured is the change of displacement of the crack faces, and this must be related to the compliance through a nonlinear calibration function and an assumed crack geometry. For NT-4, this is a circumferential crack and the relationship is (Tada *et al*. 1985)

$$\frac{\delta_a}{\Delta P} = \frac{4\sigma a}{(1 - a/r)^2}\frac{1 - \nu}{E}, \tag{4.5}$$

where δ_a is the crack opening at the root of the notch, ν is the Poisson's ratio, E is Young's modulus, and

$$D\left(\frac{a}{r}\right) = \left(1.454 - 2.49\left[\frac{a}{r}\right] + 1.155\left[\frac{a}{r}\right]^2\right),$$

and the other terms have the same meanings as before. Figure 10 plots the crack length determined from equation (4.4) as a function of the number of fatigue cycles experienced by NT-4. At the end of fatigue crack growth, the depth of this hypothetical circumferential crack was determined via compliance measurements to be 0.70 mm. As discussed above, the tomography results show that the crack grew 0.48 mm into one side of the sample from the 0.50 mm deep notch; a circumferential

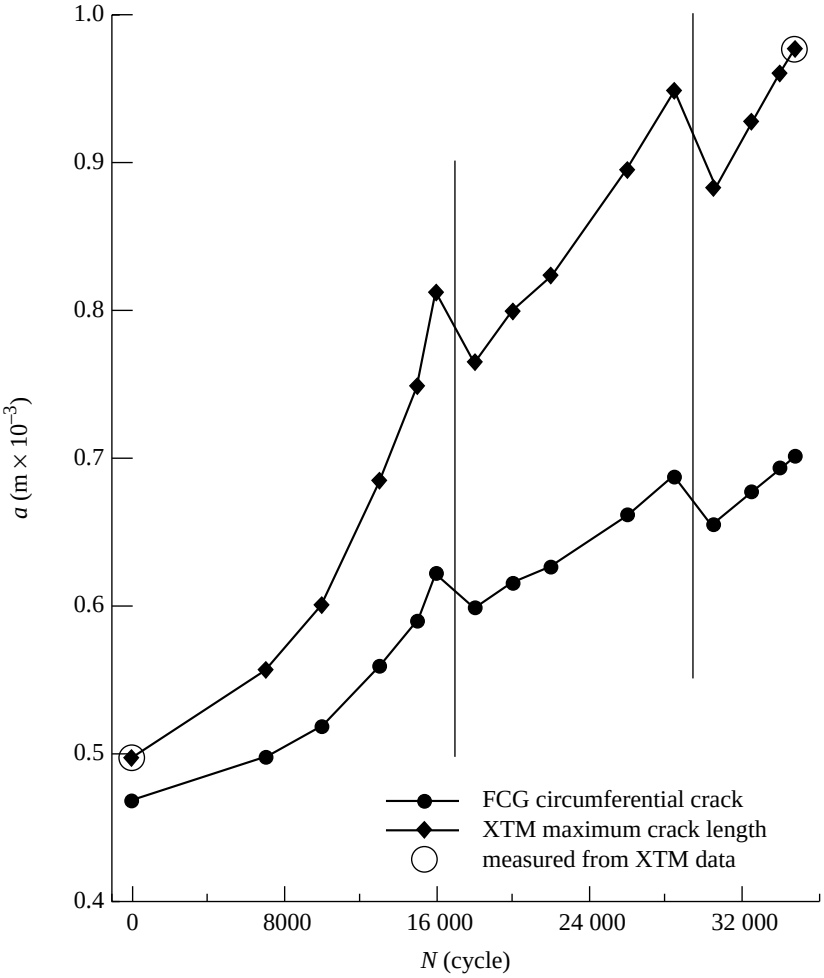

Figure 10. Crack length a_i determined from the change of compliance plotted as a function of number of cycles N_i. The vertical bars indicate changes in the applied stress.

crack of 0.74 mm in a 2.9 mm cylindrical bar was taken in the stress intensity factor calculation as being equivalent to the actual crack. The results of the compliance measurements are, therefore, consistent with the approximation of the tomography results used in calculating the stress intensity for the crack.

Crack growth rates as a function of cycle can be determined from figure 10. For each measurement of crack length a_i after cycle N_i, the crack growth rate can be approximated by

$$\left(\frac{\Delta a}{\Delta N}\right)_i \approx \frac{a_{i+1} - a_{i-1}}{N_{i+1} - N_{i-1}}.$$

While more precise methods of calculating $\mathrm{d}a/\mathrm{d}N$ could be used, the approximation of the actual crack by a circumferential crack does not warrant using an approach more complex than that given here. Load shedding was used to avoid catastrophic crack propagation, and the vertical lines in figure 10 indicate where the applied load

was changed: from 55 to 50 kg after cycle 18 000, and from 50 to 45 kg after cycle 30 500. The decrease in crack growth rate following each instance of load shedding is clear. Accordingly, the formula for $\Delta a/\Delta N$ can only be applied within each of the three ranges.

In figure 10 there appears to be a decrease in crack length after each instance of load shedding. This can be due to the method of measuring the change in strain; measurements made after such a drop may show a systematic, albeit slight, change in apparent crack length. The second possibility is that crack closure is causing the apparent decrease. The decrement of load during shedding (5 kg) is of the order of the increment of unloading (9 kg) during tomographic imaging. Given that $K_{\mathrm{cl}}/K_{\max}$ typically decreases with increasing crack length, and that significant physical crack closure was seen after one increment of unloading, it may be that the apparent drop in crack length is a product of crack closure.

In calculating crack propagation rates, one can seriously underestimate the velocity with which the crack tip travels if one treats the crack as if it were growing uniformly from all points of the circumferential notch. At one position in NT-4, the crack grew about twice as far into the sample as was indicated by the compliance measurements and as was assumed in the approximation of K. The left-hand open circle in figure 10 shows the initial crack length (i.e. that determined from the sample diameter) measured by tomography, and the right-hand open circle shows the 0.98 mm crack length at maximum crack penetration revealed by tomography: the 0.5 mm notch length is added to the 0.48 mm that the crack propagated. The crack propagation rates must be rescaled, therefore, to reflect local differences if the crack-tip velocity is to be computed accurately.

Figure 11 compares the crack propagation rate $\mathrm{d}a/\mathrm{d}N$ for sample NT-4 as a function of stress intensity range ΔK with results obtained on compact tension tensile samples (Guvenilir 1995). The vertical bars represent the crack growth rates for NT-4; the bottom of the bar is the rate if one assumes the crack grew uniformly around the notch, while the top of the bar indicates the maximum crack-tip rate, i.e. as revealed by tomography. Crack propagation rates can also be calculated for sample NT-3; here, the maximum local crack propagation rate inferred from the tomography measurements, and that calculated from the clip gauge output and assuming a circumferential crack, differ by a somewhat smaller amount than in NT-4. Data from NT-3 and from the literature (Yoder *et al*. 1988, 1989; Pao *et al*. 1989), also shown, agree with the present results.

Two- or three-dimensional finite-element calculations would provide a more precise estimate of crack length as a function of fatigue cycles and of the stress intensity, but the results of such calculations are expected to be close to what was presented above. It is quite difficult to measure small crack lengths accurately using conventional macroscopic methods, and the XTM data provide a more accurate determination of crack length in the interior of NT samples.

The XTM data show that opposite faces of the crack in sample NT-4 begin to contact at loads above 80% of the maximum during the fatigue cycle, i.e. at $K = 5.1\ \mathrm{MPa\,m^{-1/2}}$; this is higher than the nominal 'closure' load (15 kg, $K_{\mathrm{cl}} = 2.1\ \mathrm{MPa\,m^{-1/2}}$). The situation is quite similar in sample NT-3: the closure load is 47% of the maximum load ($K_{\mathrm{cl}} = 3.5\ \mathrm{MPa\,m^{-1/2}}$), and substantial crack-face contact began at loads above 61% of the maximum. The values of K_{cl} are different for NT-4 and NT-3, as are the ratios $K_{\mathrm{cl}}/K_{\max}$ (33% and 47%, respectively). For com-

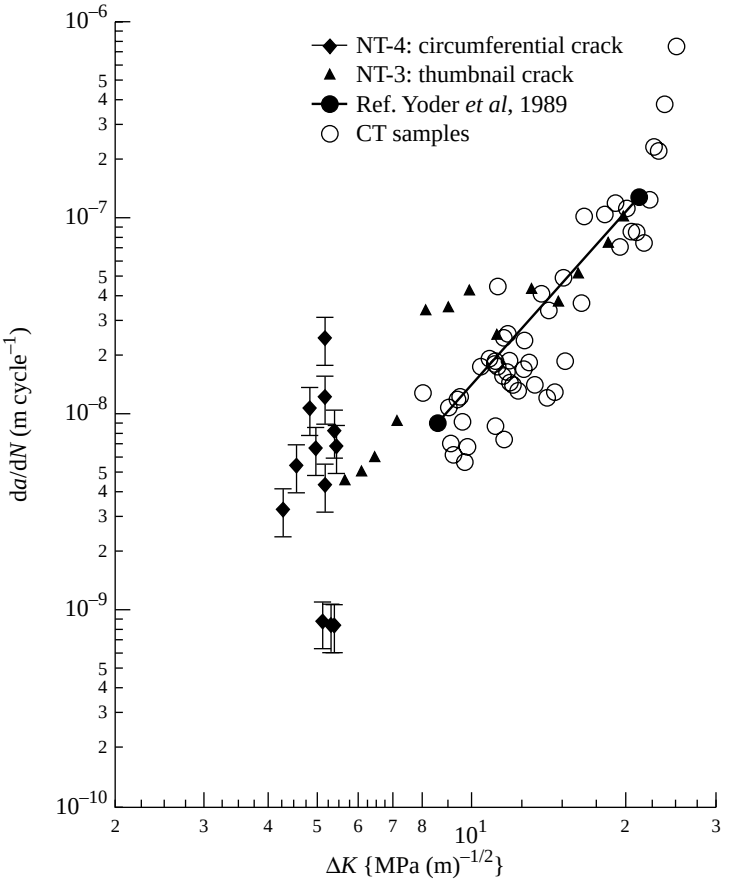

Figure 11. Comparison of da/dN versus ΔK for samples NT-4 and NT-3, and for compact tension samples. The diamonds indicate data from NT-4, the triangles are from NT-3, and the open circles are from compact tension samples from the same plate of Al–Li 2090. A summary of propagation rates from the literature is shown by the closed circles and the solid line.

parison, others have found K_{cl} to range from about 90% of $K_{\max}$ at K_{th} to about 50% of $K_{\max}$ at $K = 10\ \mathrm{MPa\,m^{-1/2}}$ for Al–Li alloys (Yoder *et al*. 1988).

The geometry of the fatigue cracks in samples NT-3 and NT-4 are quite different, as is the pattern of physical contact: in NT-4, the flatter crack appeared to zip shut rather smoothly from its tip, while in NT-3 the asperity-dominated crack had substantial contact at positions away from the crack tip before the tip retreated. Significant crack branching was seen in NT-3 but not in NT-4. Also, in NT-4, the rate of change of the fraction of voxels remaining open with decreasing load did not change abruptly as it did in NT-3. One should note, however, that the very different geometries of crack NT-3 and NT-4 resemble different portions of crack faces observed in the compact tension samples (Guvenilir *et al*. 1994; Haase *et al*. 1998). Complex interactions, therefore, appear to be at play in samples with larger dimensions, the result of which is abrupt changes of crack path in compact tension samples of Al–Li 2090.

Samples of Al–Li 2090 have pancake shaped grains (dimensions 0.05 mm × 0.5 mm

$\times$ 2.5 mm) (Venkateswara Rao *et al*. 1988*a*, *b*), and, in NT-3 and NT-4, the largest grain dimension was in the loading direction and the second largest in the crack propagation direction. On average, at least 38 grains are expected, therefore, across the notch plane perpendicular to the crack propagation direction and four are expected along the propagation direction. Microtexture has been observed to change over distances (along the crack propagation directions of samples NT-4 and NT-3) no greater than 1 mm (Stock *et al*. 1995*b*; Haase *et al*. 1998), while still being consistent with the observed macrotexture (Yoder *et al*. 1988). Not only does the orientation of the grains have the potential to influence the crack path, but also the number and arrangement of grain boundaries within the volume may be important in these samples. The work of Haase *et al*. (1998, 1999) has, in fact, demonstrated directly that this is the case in Al–Li 2090 T8E41.

5. Conclusions

High-resolution X-ray computed tomography on notched tensile sample NT-4 reveals that crack closure occurs at loads substantially above the closure load, a result in agreement with earlier observations on another Al–Li 2090 sample (NT-3). Details of the closure process for NT-3 differ, however, from those in NT-4, primarily because the crack in NT-4 is much more planar than that in NT-3. In NT-4, the crack appears to zip shut from the crack tip during the unloading portion of a fatigue cycle. This is in contrast to large amounts of contact observed away from the crack tip and on the asperities dominating the crack face in NT-3. In both samples, however, the stiffening of the samples in the lower portions of the unloading–deflection curves appears to be related to compressive loading of the portions of the crack that were already in contact. While the crack morphology is quite different in NT-3 and NT-4, much larger compact tension samples have sections where the crack face resembles NT-3 and regions where the fatigue crack appears like NT-4. Estimates of $\mathrm{d}a/\mathrm{d}N$ as a function of ΔK from both NT-3 and NT-4 are consistent with the observations of others. The processes operating in NT-3 and NT-4, therefore, appear to be representative of what occurs in larger compact tension samples.

This research was supported by the US Office of Naval Research (grants N00014-89-J-1708 and N00014-94-I-0306), and the tomography measurements were made in collaboration with Dr J. H. Kinney's group at Lawrence Livermore National Laboratory. The data for sample NT-4 were collected at the Cornell High Energy Synchrotron Source (CHESS), which is supported by the NSF. The authors thank Mr R. C. Brown of the MPRL for his help with the fatigue crack propagation experiments and Mr J. R. Cagel of the School of Materials Science and Engineering for his assistance with the computers used to analyse the data. The authors also acknowledge the help of Professor S. D. Antolovich, formerly Director of MPRL and presently at Washington State University, in initiating this research and very helpful discussions with Professor A. Saxena of MPRL and Dr G. R. Yoder of the Office of Naval Research.

References

Breunig, T. M. 1992 Nondestructive evaluation of damage in SiC/Al metal matrix composite using X-ray tomographic microscopy. PhD Thesis, Georgia Institute of Technology.

Breunig, T. M., Stock, S. R., Antolovich, S. D., Kinney, J. H., Massey, W. N. & Nichols, M. C. 1992 A framework for relating macroscopic measures and physical processes of crack closure illustrated by a study of aluminum–lithium alloy 2090. In *Fracture Mechanics: Twenty-second Symp.*, vol. I, ASTM STP 1131, pp. 749–761. Philadelphia, PA: ASTM.

Breunig, T. M., Stock, S. R. & Brown, R. C. 1993 Simple load frame for *in situ* computed tomography and X-ray tomographic microscopy. *Mater. Eval.* **51**, 596–600.

Christensen, R. H. 1963 Fatigue crack growth affected by metal fragments wedged between opening-closing crack surfaces. *Appl. Mat. Res.* October, pp. 207–210.

Elber, W. 1971 The significance of fatigue crack closure. In *Damage tolerance in aircraft structures*, ASTM STP 486, pp. 230–242. Philadelphia, PA: ASTM.

Erdogan, F. 1982 Theoretical and experimental study of fracture in pipelines containing circumferential flaws. US DOT RSPA-DMA, 50/8313, September.

Fine, M. E., Horng, J. L. & Park, D. H. 1984 Effect of microstructure and specimen geometry on crack propagation threshold. In *Fatigue 84* (ed. C. J. Beevers), vol. 2, pp. 739–748. Warley, UK: Engineering Materials Advisory Services Ltd.

Guvenilir, A. 1995 Investigation into asperity-induced closure in an Al–Li alloy using X-ray tomography. PhD Thesis, Georgia Institute of Technology.

Guvenilir, A., Stock, S. R., Barker, M. D. & Betz, R. A. 1994 Physical processes of crack closure observed in the interior of an Al–Li 2090 compact tension sample. In *4th Int. Conf. on Aluminum Alloys: Their Physical Properties and Mechanical Properties*, vol. 2, pp. 413–419.

Guvenilir, A., Breunig, T. M., Kinney, J. H. & Stock, S. R. 1997 Direct observation of crack opening as a function of applied load in the interior of a notched tensile sample of Al–Li 2090. *Acta Mater.* **45**, 1977–1987.

Haase, J. D., Guvenilir, A., Witt, J. R. & Stock, S. R. 1998 X-ray microbeam mapping of microtexture related to fatigue crack asperities in Al–Li 2090. *Acta Mater.* **46**, 4791–4799.

Haase, J. D., Guvenilir, A., Witt, J. R., Langøy, M. A. & Stock, S. R. 1999 Microtexture, asperities and crack deflection in Al–Li 2090 T8E41. In *Mixed mode crack behavior*, ASTM STP 1359, pp. 160–173. Philadelphia, PA: ASTM.

Herman, G. T. 1980 *Image reconstruction from projections: the fundamentals of computerized tomography*. Academic.

Kak, A. C. & Slaney, M. 1988 *Principles of computerized tomographic imaging*. New York: IEEE.

Kinney, J. H. & Nichols, M. C. 1992 X-ray tomographic microscopy (XTM) using synchrotron radiation. *Ann. Rev. Mater. Sci.* **22**, pp. 121–152.

Kinney, J. H., Breunig, T. M., Starr, T. L., Haupt, D., Nichols, M. C., Stock, S. R., Butts, M. D. & Saroyan, R. A. 1993 X-ray tomographic study of chemical vapor infiltration processing of ceramic composites. *Science* **260**, 789–792.

Lee, S.-B., Stock, S. R., Butts, M. D., Starr, T. L., Breunig, T. M. & Kinney, J. H. 1998 Pore geometry in woven fiber structures: 0/90 plain-weave cloth layup preform. *J. Mater. Res.* **13**, 1209–1217.

Macha, D. E., Corbly, D. M. & Jones, J. W. 1979 On the variation of fatigue-crack-opening load with measurement location. *Experimental Mech.* **19**, 207–213.

Newman Jr, J. C. & Raju, I. S. 1981 Stress intensity factor equations for cracks in three-dimensional finite bodies. NASA TM-83200. Hampton, VA: NASA Langley Research Center.

Pao, P. S., Cooley, L. A., Imam, M. A. & Yoder, G. R. 1989 Fatigue crack growth in 2090 Al–Li alloy. *Scr. Met.* **23**, 1455–1460.

Stock, S. R., Guvenilir, A., Breunig, T. M., Kinney, J. H. & Nichols, M. C. 1995*a* Computed tomography. III. Volumetric, high-resolution X-ray analysis of fatigue crack closure. *J. Metals* **47**, 19–23.

Stock, S. R., Guvenilir, A., Piotrowski, D. P. & Rek, Z. U. 1995*b* High resolution synchrotron X-ray diffraction tomography of polycrystalline samples. *Application of Synchrotron Radiation Techniques to Materials Science II, Mat. Res. Soc. Proc.* **375**, 275–280.

Suresh, S. & Ritchie, R. O. 1982 A geometric model for fatigue crack closure induced by fracture surface roughness. *Met. Trans.* A **13A**, 1627–1631.

Tada, H., Paris, P. C. & Irwin, G. R. 1985 *The stress analysis of cracks handbook*, 2nd edn. St Louis, MO: Paris.

Tokaji, K., Ando, Z., Nagae, K. & Imai, T. 1984 Effect of sheet thickness on fatigue crack retardation and validity of crack closure concept. In *Fatigue 84* (ed. C. J. Beevers), vol. 2, pp. 739–748. Warley, UK: Engineering Materials Advisory Services.

Venkateswara Rao, K. T., Yu, W. & Ritchie, R. O. 1988*a* Fatigue crack propagation in aluminum–lithium alloy 2090. Part I. Long crack behavior. *Met. Trans.* A **19A**, 549–561.

Venkateswara Rao, K. T., Yu, W. & Ritchie, R. O. 1988*b* Fatigue crack propagation in aluminum–lithium alloy 2090. Part II. Small crack behavior. *Met. Trans.* A **19A**, 563–569.

Yoder, G. R., Pao, P. S., Imam, M. A. & Cooley, M. A. 1988 Prediction of slip-band facet angle in the fatigue crack growth of an Al–Li alloy. *Scr. Met.* **22**, 1241–1244.

Yoder, G. R., Pao, P. S., Imam, M. A. & Cooley, L. A. 1989 Micromechanisms of fatigue fracture in Al–Li alloy 2090. In *Aluminum–lithium alloys. Proc. of the 5th Aluminum–Lithium Conf.* (ed. T. H. Sanders Jr & E. A. Starke Jr), pp. 1033–1041. Birmingham: Materials and Component Engineering Publications, Ltd.